DYMAT 23rd Technical Meeting

Dynamic Fracture of Ductile Materials

Implementation of GTN model in dual-horizon peridynamics

Huilong Ren[a], Xiaoying Zhuang[b,c*], Timon Rabczuk[a,d†]

[a]Institute of Structural Mechanics, Bauhaus-Universität Weimar, 99423 Weimar, Germany
[b]State Key Laboratory of Disaster Reduction in Civil Engineering, College of Civil Engineering,Tongji University, Shanghai 200092, China
[c]Institute of Conitnuum Mechanics, Leibniz University Hannover, Hannover, Germany
[d]Faculty of Civil Engineering, Ton Duc Thang University, Ho Chi Minh City, Viet Nam

Abstract

In this paper we present a dual-horizon peridynamics (DH-PD) for ductile fracture. The dual-horizon non-ordinary state-based PD is derived based on variational calculus and accounts for large deformation. The GTN model is employed to model the bulk behavior while DH-PD can naturally capture the transition from continuum to discontinuum. The penalty method is employed to suppress the zero-energy mode. Three numerical examples in three-dimensional are tested to demonstrate the capability of the method.

Keywords: Ductile fracture; dual-horizon ; GTN model ;

1. Introduction

Peridynamics (PD) has recently attracted wide attention from researchers in computational solid mechanics due to its capability to model complicated fractures. In PD, the crack is implicitly represented by the solution and not part of the problem. Hence, complex fracture patterns including crack branching and coalescence of multiple cracks

---

* Corresponding author. Tel.: +0-000-000-0000 ; fax: +0-000-000-0000 .
  E-mail address: Timon.Rabczuk@uni-weimar.de

* Corresponding author. Tel.: +0-000-000-0000 ; fax: +0-000-000-0000 .
  E-mail address: zhuang@ikm.uni-hannover.de;

are captured simply through the breakage of the bonds between material points. This avoids many techniques such as smoothing the normals of the crack surfaces in the extended finite element method (XFEM) [1], meshless methods [2] or other partition of unity methods (PUM) [3]. Also the PD is applicable for all dimensions with the unified formulation, which is not always the case in other methods [4,5]. The traditional PD method was proposed by Silling [6] in 2000 and has been exploited onwards for extensive applications of mechanical problems including impact loading, fragmentation [7,8], composites delamination[9], beam and plate structures [10,11], to name a few. An interesting alternative method is the cracking particles method [12,13,14,15] which also can handle arbitrary crack propagation without any description of the crack surface.

PD can be categorized into two types, namely, bond based peridynamics (BB-PD) where the bonds behave like independent springs, state-based peridynamics (SB-PD) where "state" means the bond deformation depends on collective deformation of other bonds. The BB-PD can only model the material with a Poisson's ratio of 1/3 in 2D or 1/4 in 3D. The state based peridynamics (SB-PD) [6,16] is an extension of BB-PD. It not only removes the Poisson's ratio restriction but also allows for complex material models. In peridynamics, the material point interacts with other material point in *horizon*, where the distances between the material points are within a threshold value. In order to remove the restriction of horizon size, the authors proposed the dual-horizon peridynamics [17,18], where any material point in the computational domain can has its horizon size, which improves the computational efficiency with minimal modification of the traditional horizon-constant PD.

Peridynamics can generally model ductile as well as brittle fracture though the majority of the publications focus on brittle fracture. The BB-PD and OSB-PD is often used to model the brittle fractures in linear solids. Ductile fracture is characterized by large deformations and nonlinear material behaviour including plastic deformations and necking. For this purpose, the NOSB-DH-PD with the famous Gurson-Tvergaard-Needleman (GTN)s model [19] is proposed in this paper.

The content of the paper is outlined as follows. In Section 2 we derive the dual-horizon PD formulation using the variational method. In Section 3, the implementation is addressed before the GTN model is described in Section 4. In Section 5, three numerical examples are presented to validate the proposed method.
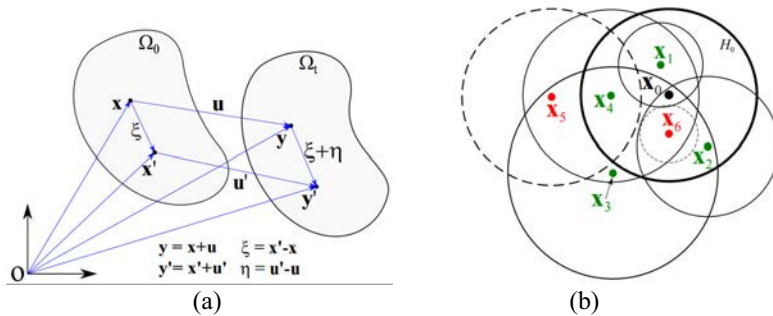
2. Variational derivation of dual-horizon peridynamics

Fig.1 (a) The configuration for deformed body. (b) Schematic diagram for horizon and dual-horizon, all circles above are horizons. $\mathcal{H}_{x_0} = \{x_1, x_2, x_4, x_6\}$ $\mathcal{H}_{x_0'} = \{x_1, x_2, x_3, x_4\}$

Consider a solid in the initial and current configuration as shown in Fig. 1(a). Let $\mathbf{x}$ be material coordinates in the initial configuration $\mathbf{\Omega}_0$; and $\mathbf{y} := \mathbf{y}(\mathbf{x}, t)$ and $\mathbf{y}' := \mathbf{y}(\mathbf{x}', t)$ are the spatial coordinates in the current configuration $\mathbf{\Omega}_t$, respectively; $\boldsymbol{\xi} := \mathbf{x}' - \mathbf{x}$ is initial bond vector, the relative distance vector between $\mathbf{x}$ and $\mathbf{x}'$; $\mathbf{u} := \mathbf{u}(\mathbf{x}, t)$ and $\mathbf{u}' := \mathbf{u}(\mathbf{x}', t)$ are the displacement vectors for $\mathbf{x}$ and $\mathbf{x}'$ respectively; $\boldsymbol{\eta} := \mathbf{u}' - \mathbf{u}$ is the relative displacement vector for bond $\boldsymbol{\xi}$; $\underline{\mathbf{Y}}\langle\boldsymbol{\xi}\rangle := \mathbf{y}(\mathbf{x}', t) - \mathbf{y}(\mathbf{x}, t) = \boldsymbol{\xi} + \boldsymbol{\eta}$ is the current bond vector for bond $\boldsymbol{\xi}$.

Horizon $\mathcal{H}_{\mathbf{x}}$ is the domain where any material point $\mathbf{x}'$ forms bond $\mathbf{x}\mathbf{x}'$ which will exerts direct force $\mathbf{f}_{\mathbf{x}\mathbf{x}'}$ on $\mathbf{x}$ and reaction force $-\mathbf{f}_{\mathbf{x}\mathbf{x}'}$ on $\mathbf{x}'$. The horizon can be viewed as direct force horizon. The horizon $\mathcal{H}_{\mathbf{x}}$ is usually presented by a spherical domain with radius of $h_{\mathbf{x}}$.

Dual-horizon is defined as a union of the points whose horizons include $\mathbf{x}$, denoted by

$$\mathcal{H}_{\mathbf{x}'} = \{\mathbf{x}' \mid \mathbf{x} \in \mathcal{H}_{\mathbf{x}'}\} \tag{1}$$

The point $\mathbf{x}'$ forms dual-bond $\mathbf{x}'\mathbf{x}$ in $\mathcal{H}_{\mathbf{x}'}$. On the other hand, $\mathbf{x}'\mathbf{x}$ is the bond formed in $\mathcal{H}_{\mathbf{x}'}$. Dual-bond $\mathbf{x}'\mathbf{x}$ will exert reaction force $-\mathbf{f}_{\mathbf{x}'\mathbf{x}}$ on point $\mathbf{x}$. In this sense, the dual-horizon can be viewed as reaction force horizons. One example to illustrate the horizon and dual-horizon is shown in Fig.1(b).

The deformation gradient $\underline{\mathbf{F}}$ for $\mathbf{x}$ is defined as

$$\underline{\mathbf{F}}_{\mathbf{x}}(\underline{\mathbf{Y}}) = \int_{\mathcal{H}_{\mathbf{x}}} w(\boldsymbol{\xi})\underline{\mathbf{Y}}\langle\boldsymbol{\xi}\rangle \otimes \boldsymbol{\xi} dV_{\mathbf{x}'} \cdot (\int_{\mathcal{H}_{\mathbf{x}}} w(\boldsymbol{\xi})\boldsymbol{\xi} \otimes \boldsymbol{\xi} dV_{\mathbf{x}'})^{-1} \tag{2}$$

The potential energy for point $\mathbf{x}$ is $W(\underline{\mathbf{Y}})$

The variation of strain energy in $\mathcal{H}$

$$\delta W(\underline{\mathbf{Y}}) = \int_{\mathcal{H}_{\mathbf{x}}} \partial_{\underline{\mathbf{Y}}} W\langle\boldsymbol{\xi}\rangle \cdot \delta \underline{\mathbf{Y}}\langle\boldsymbol{\xi}\rangle dV_{\mathbf{x}'} = \int_{\mathcal{H}_{\mathbf{x}}} \partial_{\underline{\mathbf{Y}}} W\langle\boldsymbol{\xi}\rangle \cdot (\delta \mathbf{u}' - \delta \mathbf{u}) dV_{\mathbf{x}'} \tag{3}$$

The external work in time interval $[t_1, t_2]$ is $W^{ext} = \int_{t_1}^{t_2} \int_{\Gamma_0} \mathbf{f}_0 \cdot \mathbf{u} d\Gamma_0 dt$

The Lagrangian for the system includes the kinetic energy, potential energy (strain energy, the body force energy and external work), and is expressed as

$$L(\dot{\mathbf{u}}, \mathbf{u}) = \int_{\Omega_0} \left(\frac{1}{2}\rho \dot{\mathbf{u}} \cdot \dot{\mathbf{u}} - W(\underline{\mathbf{Y}}) + \mathbf{b}_0 \cdot \mathbf{u}\right) dV_{\mathbf{x}} + \int_{\Gamma_0} \mathbf{f}_0 \cdot \mathbf{u} d\Gamma_0 \tag{4}$$

The integral of the Lagrangian L between two instants of time t_1 and t_2 is $S = \int_{t_1}^{t_2} L(\dot{\mathbf{u}}, \mathbf{u}) dt$. Applying the principle of least action, we have

$$\delta S = \int_{t_1}^{t_2} \int_{\Omega_0} \left(\rho \dot{\mathbf{u}} \cdot \delta \dot{\mathbf{u}} - \delta W(\underline{\mathbf{Y}}) + \mathbf{b}_0 \cdot \delta \mathbf{u}\right) dV_{\mathbf{x}} dt + \int_{t_1}^{t_2} \int_{\Gamma_0} \mathbf{f}_0 \cdot \delta \mathbf{u} d\Gamma_0 dt$$

$$= \int_{t_1}^{t_2} \int_{\Omega_0} \left(-\rho \ddot{\mathbf{u}} \cdot \delta \mathbf{u} - \int_{\mathcal{H}_{\mathbf{x}}} \partial_{\underline{\mathbf{Y}}} W\langle\boldsymbol{\xi}\rangle \cdot (\delta \mathbf{u}' - \delta \mathbf{u}) dV_{\mathbf{x}'} + \mathbf{b}_0 \cdot \delta \mathbf{u}\right) dV_{\mathbf{x}} dt \tag{5}$$

$$= \int_{t_1}^{t_2} \int_{\Omega_0} \left(\left(-\rho \ddot{\mathbf{u}} + \int_{\mathcal{H}_{\mathbf{x}}} \partial_{\underline{\mathbf{Y}}} W\langle\boldsymbol{\xi}\rangle dV_{\mathbf{x}'} - \int_{\mathcal{H}_{\mathbf{x}'}} \partial_{\underline{\mathbf{Y}}} W'\langle-\boldsymbol{\xi}\rangle dV_{\mathbf{x}'} + \mathbf{b}_0\right) \cdot \delta \mathbf{u}\right) dV_{\mathbf{x}} dt$$

The derivation considers the boundary condition $\delta \mathbf{u}(t_1) = 0, \delta \mathbf{u}(t_2) = 0, \delta \mathbf{u}(\Gamma_0) = 0$. In the second and third step, the dual-horizon is considered. For any $\delta \mathbf{u}$, the first order variation $\delta S = 0$ leads to

$$\rho \ddot{\mathbf{u}}_{\mathbf{x}} = \int_{\mathcal{H}_{\mathbf{x}}} \partial_{\underline{\mathbf{Y}}} W\langle\boldsymbol{\xi}\rangle dV_{\mathbf{x}'} - \int_{\mathcal{H}_{\mathbf{x}'}} \partial_{\underline{\mathbf{Y}}} W'\langle-\boldsymbol{\xi}\rangle dV_{\mathbf{x}'} + \mathbf{b}_0 \tag{6}$$

The first Piola-Kirchhoff stress $\mathbf{P}$ related to the deformation gradient is given by

$$\mathbf{P} = \partial_{\underline{\mathbf{F}}} W(\underline{\mathbf{F}}) \tag{7}$$

Using Eq. (2) and Eq. (7), we have

$$\partial_{\underline{\mathbf{Y}}} W\langle\boldsymbol{\xi}\rangle = \partial_{\underline{\mathbf{F}}} W \cdot \partial_{\underline{\mathbf{Y}}} \underline{\mathbf{F}}\langle\boldsymbol{\xi}\rangle = \mathbf{P} \cdot w(\boldsymbol{\xi})\mathbf{K}^{-1} \cdot \boldsymbol{\xi} = w(\boldsymbol{\xi})\mathbf{P}\mathbf{K}^{-1}\boldsymbol{\xi} \tag{8}$$

Therefore,

$$\partial_{\underline{y}}W\langle\xi\rangle = w(\xi)\mathbf{P_x}\mathbf{K_x^{-1}}\cdot\xi, \partial_{\underline{Y}}W'\langle-\xi\rangle = w(-\xi)\mathbf{P_x}\mathbf{K_{x'}^{-1}}\cdot(-\xi), \tag{9}$$

where

$$\mathbf{K_x} = \int_{\mathcal{H_x}} w(\xi)\xi\otimes\xi dV_{x'} \tag{10}$$

This lead to the final equation of motion of the dual-horizon non-ordinary state-based peridynamics formulation:

$$\rho\ddot{\mathbf{u}}_\mathbf{x} = \int_{\mathcal{H_x}} w(\xi)\mathbf{P_x}\mathbf{K_x^{-1}}\cdot\xi dV_{x'} + \int_{\mathcal{H'_x}} w(-\xi)\mathbf{P_x}\mathbf{K_{x'}^{-1}}\cdot\xi dV_{x'} + \mathbf{b}_0 \tag{11}$$

3. Implementation

When the deformation gradient in non-ordinary state-based PD is obtained by Eq.(2), the Cauchy stress tensor can be obtained through the standard Piola transformations. Following Ref.[20], we decompose the deformation gradient $\mathbf{F}$ into

$$\mathbf{F(x)} = \mathbf{V(x)}\cdot\mathbf{R(x)} \tag{12}$$

Where $\mathbf{V(x)}$ is the stretch tensor, $\mathbf{R(x)}$ is a proper orthogonal rotation tensor. The velocity gradient is

$$\mathbf{L} = \dot{\mathbf{F}}\mathbf{F}^{-1} \tag{13}$$

The Cauchy stress tensor is then obtained by the following steps:

Step 1. Calculate $\mathbf{D}$ and $\mathbf{W}$ based on $\mathbf{D} = \frac{1}{2}(\mathbf{L} + \mathbf{L}^T)$ and $\mathbf{W} = \frac{1}{2}(\mathbf{L} - \mathbf{L}^T)$.

Step 2. Compute

$$z_i = -e_{ijk}D_{jm}V_{mk}, \qquad \boldsymbol{\omega} = \mathbf{w} + [\mathbf{I}\,\mathrm{tr}(\mathbf{V}) - \mathbf{V}]^{-1}\mathbf{z}, \qquad \Omega_{ij} = -e_{ijk}\omega_k. \tag{14}$$

Step 3. Update the rigid rotation tensor $\mathbf{R}_{t+\Delta t}$,

$$\mathbf{R}_{t+\Delta t} = (\mathbf{I} - \frac{1}{2}\Delta t\boldsymbol{\Omega})^{-1}(\mathbf{I} + \frac{1}{2}\Delta t\boldsymbol{\Omega})\mathbf{R}_t. \tag{15}$$

Step 4. Calculate the rate of stretch tensor and update the $\mathbf{V}_{t+\Delta t}$,

$$\dot{\mathbf{V}} = \mathbf{LV} - \mathbf{V}\boldsymbol{\Omega}, \qquad \mathbf{V}_{t+\Delta t} = \mathbf{V}_t + \Delta t\,\dot{\mathbf{V}}_{\Delta t}. \tag{16}$$

Step 5. Compute the strain rate in unrotated configuration,

$$\mathbf{d} = \mathbf{R}^T\mathbf{DR}. \tag{17}$$

Step 6. Integrate the stress based on GTN damage model,

$$\boldsymbol{\sigma} = \mathbf{f}(\mathbf{d},\boldsymbol{\sigma}). \tag{18}$$

Step 7. Compute the Cauchy stress $\mathbf{T}$ and the first Piola-Kirchhoff stress $\mathbf{P}$

$$\mathbf{T} = \mathbf{R}\boldsymbol{\sigma}\mathbf{R}^T, \qquad \mathbf{P} = \det(\mathbf{F})\mathbf{TF}^{-T}. \tag{19}$$

Step 8. Using Eq.(11) to calculate the bonds force for each material point.

3.1. Control of zero-energy mode

A penalty approach that deviates from regularized deformation gradient is used to suppress the zero-energy modes [21]. The predicted location for point $\mathbf{x}'$ is

$$\mathbf{y}'^* = \mathbf{x} + \mathbf{F_x}\xi. \tag{20}$$

The hourglass vector, which denotes the difference between the predicted position $\mathbf{y}'^*$ and the actual position $\mathbf{y}'$, is calculated by

$$\mathbf{h} = \mathbf{y}'^* - \mathbf{y}'. \tag{21}$$

The hourglass vector projected onto bond

$$\gamma_{hg} = \mathbf{h} \cdot \boldsymbol{\xi}. \tag{22}$$

The hourglass force vector is defined as [21]

$$\mathbf{f}_{\mathbf{xx'}}^{hg} = -C_{hg} c \frac{\gamma_{hg}}{|\boldsymbol{\xi}|} \frac{\boldsymbol{\xi} + \boldsymbol{\eta}}{|\boldsymbol{\xi} + \boldsymbol{\eta}|}, \tag{23}$$

where $C_{hg} = 0.5$ is used in the paper, c is the microelastic modulus based on bond-based peridynamics. In the present study, $c = 18K / (\pi \delta^4)$ [22] for three dimensions.

4. GTN damage model

The GTN damage model [23,19] which considers the processes of void nucleation, growth and coalescence, is given as

$$\phi(\sigma_e, p, V_f) = \left(\frac{\sigma_e^2}{Y^2} + 2q_1 f^* \cosh\left(\frac{3}{2} q_2 \frac{p}{Y}\right) - (1 + q_3 f^{*2}) \right)^{1/2}, \tag{24}$$

where q_1, q_2, q_3, f^*, Y are model parameters influencing the form of the yield surface. f_0, f_c, f_F, f_n are the initial void volume fraction, critical void volume fraction, the failure void volume fraction. f^* is a function that quantifies the loss of strength resulting from void growth. σ_e, p and f^* are calculated by

$$\sigma_e = \sqrt{\frac{3}{2} \sigma_{ij}^D \sigma_{ij}^D}, \quad p = \sigma_{kk} / 3, \quad \sigma_{ij}^D = \sigma_{ij} - \frac{1}{3} \sigma_{kk} \delta_{ij}, \tag{25}$$

$$f^* = \begin{cases} V_f & V_f < f_c \\ f_c + \dfrac{\overline{f}_F - f_c}{f_F - f_c} (V_f - f_c) & f_c < V_f < f_F \\ \overline{f}_F & V_f > f_F \end{cases}, \tag{26}$$

where

$$\overline{f}_F = \frac{q_1 + \sqrt{q_1^2 - q_3}}{q_3}. \tag{27}$$

If $\phi > 0$ the deviatoric and volumetric plastic strain rates $\dot{\varepsilon}^{dev}, \dot{\varepsilon}^v$ are calculated using Newton-Raphson iteration method. $\overline{\varepsilon}_{matrix}$, the total accumulated plastic strain in the matrix, evolves according to.

$$\dot{\overline{\varepsilon}}_{matrix} = \frac{p\dot{\varepsilon}^v + \sigma_e \dot{\varepsilon}^{dev}}{(1 - V_f)Y}. \tag{28}$$

The evolution of the void volume fraction V_f is given by

$$\dot{V}_f = (1 - V_f)\dot{\varepsilon}^v + A_n \dot{\overline{\varepsilon}}_{matrix}, \tag{29}$$

where $A_n = \dfrac{f_N}{s_N \sqrt{2\pi}} \exp\left(-\dfrac{1}{2}\left(\dfrac{\overline{\varepsilon}_{matrix} - \varepsilon_N}{s_N}\right)^2\right)$, f_N, s_N, ε_N are material properties controlling the rate of void nucleation with plastic strain. More details are found in [24].

5. Numerical examples

5.1. Kalthoff-Winkler experiment

The Kalthoff-Winkler experiment is a classical benchmark problems for dynamic fracture[25,26,27,28]. This example aims to show the capability of DH-PD in modeling the dynamic brittle fractures. The dimension of the plate is depicted in Fig. 2(a). The thickness of the specimen is 0.01m. The material parameters used are the elastic modulus E=190GPa, ρ = 7800 kg/m^3, ν =0.25 and the energy release rate G_0=6.9e4 J/m^2. The impact loading was imposed by applying an initial velocity at v_0=22 m/s to the first three layers of particles in the domain as shown in Fig. 2(a); all other boundaries are free. The plate is discretized with two different particle sizes, namely $\Delta x_1 = 1.5625 \times 10^{-3}$ m for the coarse subdomain and $\Delta x_2 = 0.5 \Delta x_1 = 7.8125 \times 10^{-4}$ m for the fine subdomain located in the left down corner of the model, see Fig. 2(a). The total number of particles is 57,968.

The crack starts to propagate at 26.3 μs . The highest crack speed in the simulation is 1530 m/s, about 54.4% of the Rayleigh speed(2799.2 m/s). The crack patterns are nearly symmetrical, as shown in Figs 2(b). The crack propagates initially at an angle of 65.7° in the fine subdomain with respect to the original crack and 65.8° in coarse subdomain. The crack propagation angle agrees with that by Cracking particle method and Extended finite element method [28,26].
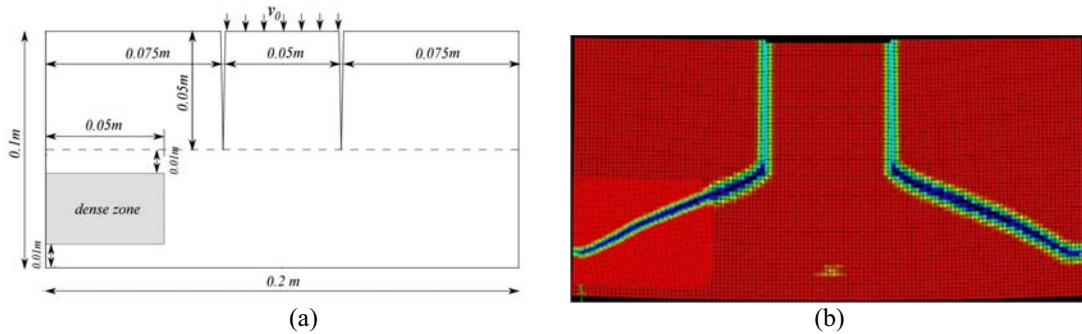

(a)   (b)

Fig. 2. (a) The setup of the specimen. (b) The crack pattern of Kalthoff-Winkler simulation by the present dual-horizon peridynamics at step 875.

5.2. Necking of a bar

Table. 1 The material parameters for GTN model

ID	E(Pa)	υ	Y (Pa)	$\dot{\varepsilon}_0$	m	q_1	q_2	q_3	f_N	s_N	e_n	f_c	f_F	f_0
Mat$_1$	1000	0.3	0.8	10.01	5	1.25	1	1.25	0.05	0.1	0.05	0.15	0.25	0
Mat$_2$	2.11e11	0.3	4.65e8	1	1	1.5	1	1.5	0.0008	0.1	0.3	0.015	0.1	1.2E-4

The horizon size is selected as $h_i = 3.015 \Delta x_i$. The variable horizons can greatly reduce the number of material points, thus improve the computational efficiency. The material is Mat$_1$ in Table 1. The bar is discretized with two type of grid spacing. The dimension of the bar is 1x1/3x1/3 m^3. A constant velocity of v_x=0.05 m/s is applied at the end of the bar while the other end is fixed. The necking happened naturally at the center of the bar. The load-displacement curve is shown in Fig.3(d).
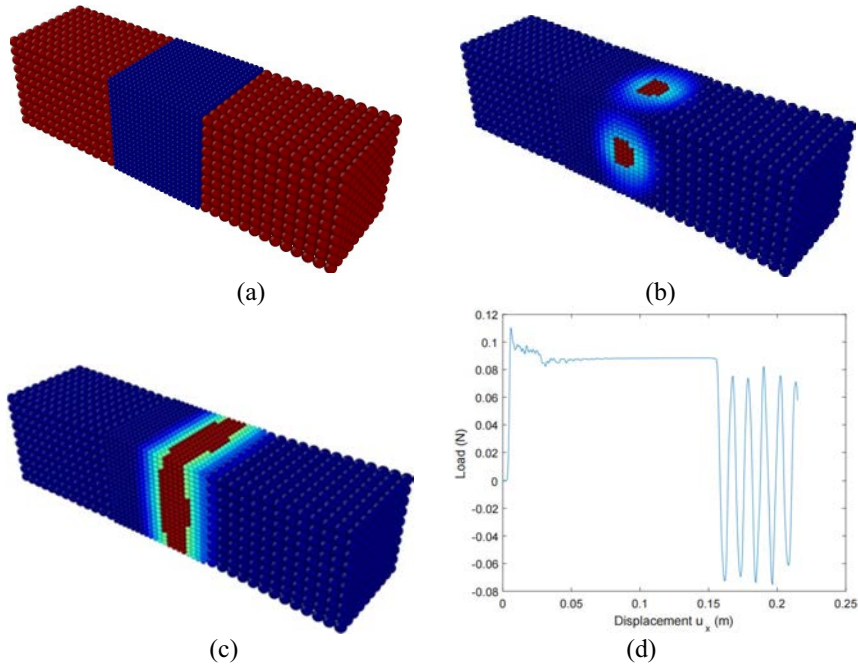
(a)

(b)

(c)

(d)

Fig. 3. (a). Discretization.(b) Damage starts from the center of the bar. (c) Total failure. (d). The load-displacement curve.

5.3. Cup-cone fracture in a round tensile bar

The material for the tensile bar is Mat$_2$ in Table 1. The maximum load is 2.682e4 N. The constant velocity of v_x=0.1 m/s at both ends but with opposite directions is applied. The dimensions and the results are shown in Fig.4(a).
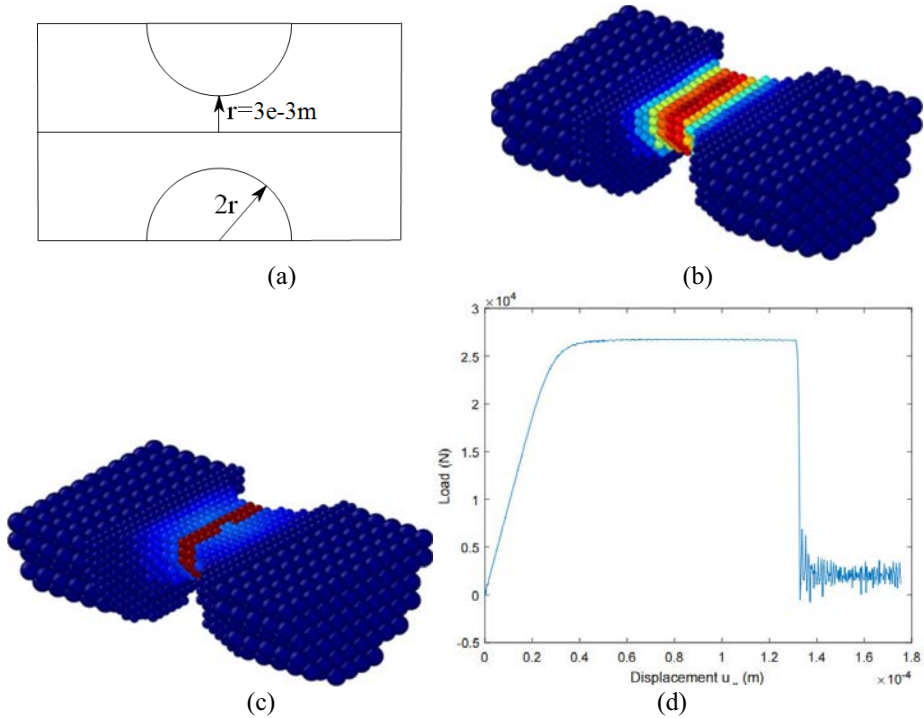

r=3e-3m

2r

(a)

(b)

(c)

(d)

Fig. 4. (a). Dimensions of the bar.(b) Void fraction distribution at the failure stage. (c) damage distribution. (d). The load-displacement curve.

6. Conclusions

In this paper, we presented a dual-horizon non-ordinary state-based peridynamics. We implemented the GTN model to simulate ductile fracture involving large deformation including plasticity. Three numerical examples are presented to validate the method.

Acknowledgements

References

[1] T. Belytschko, N. Moe¨s, S. Usui, C. Parimi, Arbitrary discontinuities in finite elements, International Journal for Numerical Methods in Engineering 50 (4) (2001) 993–1013.

[2] T. Rabczuk, G. Zi, S. Bordas, On three-dimensional modelling of crack growth using partition of unity methods, Computers & Structures 88 (2010) 1391–1411.

[3] I. Babusˇka, J. Melenk, The partition of the unity finite element method, Tech. Rep. BN-1185, Institute for Physical Science and Technology, University of Maryland, Maryland (1995).

[4] K. Cheng, T. Fries, Higher-order xfem for curved strong and weak discontinuities, International Journal for Numerical Methods in Engineering.

[5] A. Gravouil, N. Moes, T. Belytschko, Non-planar 3D crack growth by the extended finite element and level sets - part ii: Level set update, International Journal for Numerical Methods in Engineering 53 (2002) 2569–2586.

[6] S. Silling, Reformulation of elasticity theory for discontinuities and long-range forces, Journal of the Mechanics and Physics of Solids 48 (1) (2000) 175–209.

[7] X. Lai, B. Ren, H. Fan, S. Li, C. Wu, R. A. Regueiro, L. Liu, Peridynamics simulations of geomaterial fragmentation by impulse loads, International Journal for Numerical and Analytical Methods in Geomechanics.

[8] W. Gerstle, N. Sau, S. Silling, Peridynamic modeling of concrete structures, Nuclear engineering and design 237 (12) (2007) 1250–1258.

[9] E. Oterkus, E. Madenci, O. Weckner, S. Silling, P. Bogert, A. Tessler, Combined finite element and peridynamic analyses for predicting failure in a stiffened composite curved panel with a central slot, Composite Structures 94 (2012) 839–850.

[10] E. Moyer, M. Miraglia, Peridynamic solutions for Timoshenko beams, Engineering 6 (2014) Article ID:46262.

[11] J. OGrady, J. Foster, Peridynamic plates and flat shells: A non-ordinary, state-based model, International Journal of Solids and Structures 51 (2014) 4572–4579.

[12] T. Rabczuk, T. Belytschko, Cracking particles: a simplified meshfree method for arbitrary evolving cracks, International Journal for Numerical Methods in Engineering 61 (13) (2004) 2316–2343.

[13] T. Rabczuk, P. Areias, T. Belytschko, A simplified mesh-free method for shear bands with cohesive surfaces, International Journal for Numerical Methods in Engineering 69 (5) (2007) 993–1021.

[14] T. Rabczuk, T. Belytschko, A three dimensional large deformation meshfree method for arbitrary evolving cracks, Computer Methods in Applied Mechanics and Engineering 196 (29-30) (2007) 2777–2799.

[15] T. Rabczuk, S. Bordas, G. Zi, A three dimensional meshfree method for static and dynamic multiple crack nucleation/propagation with crack path continuity, Computational Mechanics 40 (3) (2007) 473–495.

[16] S. A. Silling, M. Epton, O. Weckner, J. Xu, E. Askari, Peridynamic states and constitutive modeling, Journal of Elasticity 88 (2) (2007) 151–184.

[17] H. Ren, X. Zhuang, Y. Cai, T. Rabczuk, Dual-horizon peridynamics, International Journal for Numerical Methods in Engineering.

[18] H. Ren, X. Zhuang, T. Rabczuk, Dual-horizon peridynamics: A stable solution to varying horizons, Computer Methods in Applied Mechanics and Engineering 318 (2017) 762–782.

[19] V. Tvergaard, A. Needleman, Analysis of the cup-cone fracture in a round tensile bar, Acta Metallurgica 32 (1) (1984) 157 – 169. doi:http://dx.doi.org/10.1016/0001-6160(84)90213-X.
URL   http://www.sciencedirect.com/science/article/pii/000161608490213X

[20] D. Flanagan, L. Taylor, An accurate numerical algorithm for stress integration with finite rotations, Computer methods in applied mechanics and engineering 62 (3) (1987) 305–320.

[21] D. J. Littlewood, A nonlocal approach to modeling crack nucleation in aa 7075-t651, in: ASME 2011 International Mechanical Engineering Congress and Exposition, American Society of Mechanical Engineers, 2011, pp. 567–576.

[22] S. Silling, E. Askari, A meshfree method based on the peridynamic model of solid mechanics, Computers & structures 83 (17) (2005) 1526–1535.

[23] A. L. Gurson, et al., Continuum theory of ductile rupture by void nucleation and growth: Part iłyield criteria and flow rules for porous ductile media, Journal of engineering materials and technology 99 (1) (1977) 2–15.

[24] L. Malcher, F. A. Pires, J. C. de S¢, An extended GTN model for ductile fracture under high and low stress triaxiality, Interna- tional Journal of Plasticity 54 (2014) 193 – 228. doi:https://doi.org/10.1016/j.ijplas.2013.08.015.
URL   http://www.sciencedirect.com/science/article/pii/S0749641913001708

[25] S. Li, W. K. Liu, A. J. Rosakis, T. Belytschko, W. Hao, Mesh-free galerkin simulations of dynamic shear band propagation and failure mode transition, International Journal of solids and structures 39 (5) (2002) 1213–1240.

[26] T. Belytschko, H. Chen, J. Xu, G. Zi, Dynamic crack propagation based on loss of hyperbolicity and a new discontinuous enrichment, International Journal for Numerical Methods in Engineering 58 (12) (2003) 1873–1905.

[27] J.-H. Song, P. M. Areias, T. Belytschko, A method for dynamic crack and shear band propagation with phantom nodes, Interna- tional Journal for Numerical Methods in Engineering 67 (6) (2006) 868–893.

[28] T. Rabczuk, G. Zi, S. Bordas, H. Nguyen-Xuan, A simple and robust three-dimensional cracking-particle method without enrich- ment, Computer Methods in Applied Mechanics and Engineering 199 (37) (2010) 2437–2455.